
PERGAMON

Journal of Quantitative Spectroscopy & Radiative Transfer 72 (2002) 691–713

Journal of Quantitative Spectroscopy & Radiative Transfer

www.elsevier.com/locate/jqsrt

Optical tomography using the time-independent equation of radiative transfer — Part 1: forward model

Alexander D. Klose[a,b], Uwe Netz[b], Jürgen Beuthan[b], Andreas H. Hielscher[a,c,*]

[a] *Department of Pathology, State University of New York Downstate Medical Center, 450 Clarkson Avenue, Brooklyn, NY 11203, USA*

[b] *Institut für Medizinische Physik, Klinikum Benjamin Franklin, Freie Universität Berlin, Fabeckstr. 60-62, 14195 Berlin, Germany*

[c] *Department of Electrical and Computer Engineering, Polytechnic University, 5 Metrotech Center, Brooklyn, NY 11201, USA*

Received 3 January 2001; accepted 20 March 2001

Abstract

The presented study consists of two parts. The overall goal is to introduce and experimentally test a novel optical tomographic imaging algorithm that is based on the equation of radiative transfer. Using the equation of radiative transfer rather than the diffusion equation permits the consideration of highly scattering media that contain void-like regions that have very low absorption and scattering coefficients. In part I we concentrate on the detailed description and evaluation of a numerical forward model that accurately describes photon propagation in such media. In part II we focus on the inclusion of this forward model into a model-based iterative image reconstruction (MOBIIR) scheme. Using the MOBIIR scheme one can determine the spatial distribution of optical properties inside highly scattering media from measurements acquired on the surface of the medium. The mathematical and numerical background for the reconstruction algorithm, especially the adjoint differentiation scheme for the gradient calculation, will be presented. The code is tested with experimental data from tissue-phantoms that contain water-filled, void-like regions.

The forward model to be described in part I is based on an upwind-difference discrete-ordinate formulation of the time-independent equation of radiative transfer. The upwind-difference representation has the advantage that it provides a convenient mathematical framework for calculating the derivative of the fluence with respect to the optical parameters using an adjoint differentiation technique, to be described in part II. The performance of the forward model is tested with experimental data obtained from homogeneous tissue-phantoms and from phantoms that contain void-like regions. We find good agreement

* Corresponding author. The author is now with the Departments of Biomedical Engineering and Radiology, Columbia University, 416 CEPSR-Schapiro Bldg. Mail Code 8904, 530 West 1120th Street, New York, NY 10027, USA. Tel.: +1-212-854-4460; fax: +1-212-854-8725.

E-mail address: ahielscher@downstate.edu (A.H. Hielscher).

PII: S0022-4073(01)00150-9

between experimental measurements and theoretical predictions of the measurements.

Keywords: Equation of radiative transfer; Transport theory; Photon propagation; Scattering media; Discrete-ordinate method; Finite-difference method; Upwind-difference scheme

1. Introduction

Optical tomography (OT), also referred to as diffuse optical tomography (DOT), or photon migration tomography (PMT), has made considerable advances in recent years [1–3]. In this technique near-infrared light in the wavelength region of approximately $650\,\text{nm} < \lambda < 900\,\text{nm}$ is used to illuminate highly scattering media. Based on measurements of transmitted and/or reflected intensities on the surface of the medium, a reconstruction of the spatial distribution of the optical properties (e.g. absorption coefficient, μ_a, and scattering coefficient, μ_s) inside the medium is attempted. While similar problems can be found in many different scientific areas, ranging from oceanography and atmospheric science, to astronomy and neutron physics, the recent advances in OT have mainly been driven by applications in biomedical optics. This field is concerned with the use of visible and near-infrared light for diagnosis and treatment of biological tissues. Examples include optical monitoring of blood oxygenation [4,5], detection of cerebral hemorrhages [6,7], functional imaging of brain activity [8–10], and diagnosis of Alzheimer's disease [11,12], rheumatoid arthritis [13,14], or cancer [15–17]. These applications rely on the fact that various disease processes and most physiological changes affect the optical properties of biological tissue. The optical properties of interest are the absorption coefficient μ_a, the scattering coefficient μ_s, and the anisotropy factor g, or a combination thereof. The differences in these optical properties between healthy and pathological tissues provide the contrast for this imaging technology.

Because near-infrared light is strongly scattered in tissue, standard backprojection techniques [18] as applied in X-ray tomography have been of limited success [19,20]. Therefore, most groups are currently employing so-called model-based iterative imaging reconstruction (MOBIIR) techniques [21–45]. These techniques employ a forward model that provides predictions of the detector readings based on a guess of the distribution of optical properties inside the medium. The predicted detector readings are compared with experimental data using an appropriately defined objective function. The true distribution of optical properties is determined by iteratively updating the guess and performing new forward calculations with these updated optical properties until the predicted data agree with the detector readings. The final distribution of optical properties is displayed as an image.

It is clear that the quality of the reconstructed image depends strongly on the accuracy of the forward model. If the forward model does not accurately describe the propagation of photons inside the medium, the model-based reconstruction scheme will fail. At present, most algorithms rely on the validity of the diffusion approximation to the more generally applicable equation of radiative transfer [46–54]. While in many cases this is indeed a good approximation for describing light propagation in biological tissues, several researchers have theoretically and experimentally determined what the limits of this approximation are [55–57]. For example, it

was shown that the diffusion approximation fails when the medium contains regions in which the absorption coefficient is not much smaller than the scattering coefficient, or regions in which the scattering and absorption are very low, so-called void-like regions. Turbid media that contain void-like areas play an important role in several biomedical imaging applications. For example, the highly scattering brain tissue is enclosed in a layer of almost clear cerebrospinal fluid, which has very low scattering and absorption coefficients. How this layer effects light propagation has recently been the subject of many studies and discussions [57–62]. Another example is the almost clear synovial fluid in joints [13,14,63].

Some groups have attempted to overcome the disadvantages of diffusion-equation-based schemes. For example Arridge et al. presented a hybrid radiosity-diffusion approach for handling non-scattering regions with diffusing domains [64,65]. The method treats light propagation in highly scattering regions with the diffusion approximation and uses a ray-tracing method for the void areas. However, this approach does not address highly absorbing regions, and it requires a priori knowledge about the exact position of the void-like regions. Therefore, this approach appears to be of limited use for optical tomography, even though the results of the forward calculations are impressive [59,60].

In another study [66], Dorn recently reported on a so-called transport-backtransport method. He applied this non-linear inversion method to the two-dimensional time-dependent equation of radiative transfer, and used a finite-difference discrete-ordinates method to describe photon propagation in a heterogeneous medium with non-reentry boundary conditions. Using synthetic data, he showed in numerical studies that this approach is capable of reconstructing scattering and absorbing inhomogeneities inside turbid media. However, Dorn did not consider void-like regions in his work. Furthermore, the algorithm was not compared with experimental data. In this case the refractive index mismatch at the tissue–air boundary has to be considered, and the non-reentry boundary condition needs to be modified.

Our group reported in earlier studies on a radiative-transfer-based forward model, which is part of a MOBIIR scheme [41]. That algorithm employed an upwind-difference discrete-ordinates method applied to the two-dimensional time-dependent equation of radiative transfer. A Jacobi method was used to solve the associated matrix equation. Time-independent results were obtained by using a time-independent source term. Photon propagation was described in isotropically scattering media with non-reentry boundary conditions. Numerical results were presented that showed the reconstructed spatial distribution of the scattering coefficient.

In this work we extend our previous code to include anisotropically scattering media. Furthermore, a boundary condition that is capable of describing the refractive index mismatch at the tissue–air boundary is included. In this way, it is for the first time possible to test the algorithm with experimental data from well-characterized tissue phantoms, something that has not been done previously. Furthermore, the discretized time-independent equation of radiative transfer is solved with a successive over-relaxation (SOR) method. This considerably accelerates the rate of convergence of the algorithm, while still providing a structure amenable to adjoint differentiation (AD) techniques. AD techniques are a crucial component of the iterative image reconstruction scheme, which will be presented in part II of this study.

In part I, we describe in detail the implementation of the modified forward code, focusing on the improvements that have been made with respect to the earlier algorithm [41]. To test our forward model, we compare numerical calculations to measured data. Detailed descriptions

of the tissue phantoms and of the experimental set-up are presented. In addition to detailed studies on homogeneous media, which show the dependence of the predicted data on variations of optical properties, we pay special attention to media that contain void-like inclusions. A discussion of the results and a summary of the main findings conclude part I.

2. Numerical methods

Photon transport in scattering media can be described by the time-independent equation of radiative transfer [67–69], given by

$$\omega\nabla\Psi(\mathbf{r},\omega)+(\mu_a+\mu_s)\Psi(\mathbf{r},\omega)=S(\mathbf{r},\omega)+\mu_s\int_0^{2\pi}p(\omega,\omega')\Psi(\mathbf{r},\omega')\,d\omega'. \tag{1}$$

The fundamental quantity in radiative transport theory is the radiance $\Psi(\mathbf{r},\omega)$ at the spatial position $\mathbf{r}$, which is directed into a solid unite angle ω, with units of $W\,cm^{-2}\,sr^{-1}$. The integral of the radiance over all angles ω at one point $\mathbf{r}$ yields the fluence $\Phi(\mathbf{r})$:

$$\Phi(\mathbf{r})=\int_{2\pi}\Psi(\mathbf{r},\omega)\,d\omega. \tag{2}$$

Other quantities that are included in the transport equation are the scattering coefficient μ_s and the absorption coefficient μ_a, both given in units of cm^{-1}, and the scattering phase function $p(\omega,\omega')$. In this work we employ the commonly used Henyey–Greenstein scattering function [70],

$$p(\cos\theta)=\frac{1-g^2}{2(1+g^2-2g\cos\theta)^{3/2}}. \tag{3}$$

where θ is the angle between the two directions ω and ω'. The parameter g is called the anisotropy factor and is used to characterize the angular distribution of scattering.

Various computational techniques exist that numerically solve the equation of radiative transfer [71]. Techniques commonly applied include the singular eigenfunction method, the method of spherical harmonics, the method of characteristics, the finite-element method, and the finite-difference discrete-ordinate method. A concise review of these techniques has been presented by Sanchez and McCormick [72]. The discrete-ordinates method is widely used with several different finite-difference approximations [73,74] such as the diamond-difference scheme, the weighted diamond-difference scheme, or the centered-difference scheme [75–80]. In this paper we employ the upwind-difference scheme in connection with the discrete-ordinates method to the equation of radiative transfer [81]. This is a computationally efficient method for the calculation of the radiance and has the advantage that it easily supplies the required mathematical structure for the adjoint differentiation calculation. This adjoint calculation is a central part of the solution of the inverse problem, which is the focus of part II of this study.

To solve the equation of radiative transfer using an upwind-difference discrete-ordinates method, the angular and spatial variables have to be discretized. First, the integral term in Eq. (1) is replaced by a quadrature formula that uses a finite set of K angular directions

ω_k with $k=1,\ldots,k$. This yields a set of K coupled ordinary differential equations for the angular-dependent radiance $\Psi_k(\mathbf{r})=\Psi(\mathbf{r},\omega_k)$ in the directions ω_k. The coupling term is the internal source term $\mu_s\sum_{k'=1}^{k} a_{k'}\,p(\omega_{k'},\omega_k)\Psi(\mathbf{r},\omega')$. The parameter $a_{k'}$ is a weighting factor that depends on the chosen quadrature formula. In this work we employ the extended trapezoidal rule [82].

Additionally, the spatial variable $\mathbf{r}$ needs to be discretized. The domain Ω is defined by a rectangular spatial mesh with I grid points on the x-coordinate and J grid points on the y-coordinate. The distance between two adjacent grid points along the x-axis is Δx and along the y-axis is Δy. The angular radiance at the grid point (i,j) with position $\mathbf{r}=(x_i,y_j)$ for a particular direction ω_k is represented by $\Psi_{k,i,j}=\Psi_k(x_i,y_j)$. The angular direction ω_k can be expressed in cartesian coordinates with $\xi_k=\mathbf{e}_x\cdot\omega_k=\cos(\omega_k)$ and $\eta_k=\mathbf{e}_y\cdot\omega_k=\sin(\omega_k)$. Finally, the spatial derivatives have to be replaced with a finite-difference scheme. The upwind-difference formula depends on the direction ω_k of the angular-dependent radiance Ψ_k. Thus, the set of all angular directions ω_k are subdivided into four quadrants and we get four different difference formulas for the radiance $\Psi_{k,i,j}$, depending on the sign of ξ_k and η_k:

$$\text{I) } \xi_k>0,\eta_k>0\text{: } \frac{\partial\Psi}{\partial x}\approx\delta_x\Psi_{k,i,j}=\frac{\Psi_{i,j}-\Psi_{i-1,j}}{\Delta x},\quad \frac{\partial\Psi}{\partial y}\approx\delta_y\Psi_{k,i,j}=\frac{\Psi_{i,j}-\Psi_{i,j-1}}{\Delta y},\tag{3a}$$

$$\text{II) } \xi_k<0,\eta_k>0\text{: } \frac{\partial\Psi}{\partial x}\approx\delta_x\Psi_{k,i,j}=\frac{\Psi_{i+1,j}-\Psi_{i,j}}{\Delta x},\quad \frac{\partial\Psi}{\partial y}\approx\delta_y\Psi_{k,i,j}=\frac{\Psi_{i,j}-\Psi_{i,j-1}}{\Delta y},\tag{3b}$$

$$\text{III) } \xi_k>0,\eta_k<0\text{: } \frac{\partial\Psi}{\partial x}\approx\delta_x\Psi_{k,i,j}=\frac{\Psi_{i,j}-\Psi_{i-1,j}}{\Delta x},\quad \frac{\partial\Psi}{\partial y}\approx\delta_y\Psi_{k,i,j}=\frac{\Psi_{i,j+1}-\Psi_{i,j}}{\Delta y},\tag{3c}$$

$$\text{IV) } \xi_k<0,\eta_k<0\text{: } \frac{\partial\Psi}{\partial x}\approx\delta_x\Psi_{k,i,j}=\frac{\Psi_{i+1,j}-\Psi_{i,j}}{\Delta x},\quad \frac{\partial\Psi}{\partial y}\approx\delta_y\Psi_{k,i,j}=\frac{\Psi_{i,j+1}-\Psi_{i,j}}{\Delta y}.\tag{3d}$$

The time-independent radiative transfer equation, with the external and internal source terms on the right-hand side, can now be written as

$$\xi_k\delta_x\Psi_{k,i,j}+\eta_k\delta_y\Psi_{k,i,j}+(\mu_a+\mu_s)\Psi_{k,i,j}=S_{k,i,j}+\mu_s\sum_{k'=1}^{k}a_{k'}\,p_{k,k'}\Psi_{k',i,j}.\tag{4}$$

Recasting the left-hand side of the preceding equation as a single operator acting upon $\Psi_{k,i,j}$, we get

$$\{\xi_k\cdot\delta_x+\eta_k\cdot\delta_y+(\mu_a+\mu_s)\}\Psi_{k,i,j}=S_{k,i,j}+\mu_s\sum_{k'=1}^{k}a_{k'}\,p_{k,k'}\Psi_{k',i,j}.\tag{5}$$

For example, for a fixed k with $\xi_k>0,\eta_k>0$ this becomes

$$\xi_k\frac{\Psi_{k,i,j}-\Psi_{k,i-1,j}}{\Delta x}+\eta_k\frac{\Psi_{k,i,j}-\Psi_{k,i,j-1}}{\Delta y}+(\mu_a+\mu_s)\Psi_{k,i,j}=S_{k,i,j}+\mu_s\sum_{k'=1}^{K}a_{k'}\,p_{k,k'}\Psi_{k',i,j}\tag{6}$$

It is apparent that the system of equations (5) corresponding to all K directions can be written as a single matrix equation

$$\mathbf{A}\Psi = \mathbf{b} \tag{7}$$

The resulting system of equations for the radiance $\Psi_{k,i,i}$ for all grid points can be solved for each ordinate index k by a Gauss–Seidel method [83]. Accordingly, we split the matrix $\mathbf{A}$ into a diagonal part $\mathbf{D}$, an upper-triangular part $\mathbf{U}$, and a lower-triangular part $\mathbf{L}$, with $\mathbf{A} = \mathbf{L} + \mathbf{D} + \mathbf{U}$. The original matrix equation (6) can now be written as

$$(\mathbf{L} + \mathbf{D} + \mathbf{U})\Psi = \mathbf{b}, \tag{8a}$$

$$(\mathbf{D} + \mathbf{L})\Psi = -\mathbf{U}\Psi + \mathbf{b}. \tag{8b}$$

In our case an upper matrix U does not exist. Thus, we get for example for the case $\xi_k > 0$, $\eta_k > 0$:

$$\underbrace{\left\{\frac{\xi_k}{\Delta x} + \frac{\eta_k}{\Delta y} + (\mu_a + \mu_s)\right\}\Psi_{k,i,j}}_{\text{diagonal matrix } D} \underbrace{-\frac{\xi_k}{\Delta x}\Psi_{k,i-1,j} - \frac{\eta_k}{\Delta y}\Psi_{k,i,j-1}}_{\text{lower matrix } L} = \underbrace{S_{k,i,j} + \mu_s \sum_{k'=1}^{k} a_{k'}\, p_{k,k'}\Psi_{k',i,j}}_{b}. \tag{9}$$

Now the iterative form with the iteration matrix $(\mathbf{D} + \mathbf{L})$ is expressed as

$$(\mathbf{D} + \mathbf{L})\Psi^{z+1} = -\mathbf{U}\Psi^{z} + b, \tag{10}$$

and for the case $\xi_k > 0, \eta_k > 0$ we obtain

$$\left\{\frac{\xi_k}{\Delta x} + \frac{\eta_k}{\Delta y} + (\mu_a + \mu_s)\right\}\Psi^{z+1}_{k,i,j} - \frac{\xi_k}{\Delta x}\Psi^{z+1}_{k,i-1,j} - \frac{\eta_k}{\Delta y}\Psi^{z+1}_{k,i,j-1} = S_{k,i,j} + \mu_s \sum_{k'=1}^{k} \mathrm{a}_{k'}\, p_{k,k'}\Psi^{z}_{k',i,j}, \tag{11}$$

$$\Psi^{z+1}_{k,i,j} = \frac{\left\{S_{k,i,j} + \mu_s \sum_{k'=1}^{k} \mathrm{a}_{k'}\, p_{k,k'}\Psi^{z}_{k',i,j} + (\xi_k/\Delta x)\Psi^{z+1}_{k,i-1,j} + (\eta_k/\Delta y)\Psi^{z+1}_{k,i,j-1}\right\}}{\{\xi_k/\Delta x + \eta_k/\Delta y + (\mu_a + \mu_s)\}}. \tag{12}$$

All $\Psi^{z+1}_{k,i-1,j}$ and $\Psi^{z+1}_{k,i,j-1}$ are already calculated at the current iteration step because of the vector ordering. For all other ordinates ω_k besides $\xi_k > 0$, $\eta_k > 0$, the radiance vector Ψ has to be re-ordered to get the same matrix structure with $(\mathbf{D} + \mathbf{L})\Psi = -\mathbf{U}\Psi + \mathbf{b}$. The iteration process is repeated until the error norm $E = ||\Psi^{z+1}_{k,i,j} - \Psi^{z}_{k,i,j}||$ at the grid point (i,j) is smaller than a defined ε.

A significant improvement in convergence speed can be achieved by a slight modification to the Gauss–Seidel method. The SOR method uses a relaxation parameter ρ with $1 < \rho < 2$ in order to correct the solution $\Psi^{z+1}_{k,i,j}$ of the Gauss–Seidel iteration, now denoted as $\bar{\Psi}^{z+1}_{k,i,j}$. The updated value $\Psi^{z+1}_{k,i,j}$ of the SOR is a linear combination of the Gauss–Seidel value $\bar{\Psi}^{z+1}_{k,i,j}$ and the previously computed value $\Psi^{z}_{k,i,j}$ of the SOR using

$$\Psi^{z+1}_{k,i,j} = (1-\rho)\Psi^{z}_{k,i,j} + \rho\bar{\Psi}^{z+1}_{k,i,j}. \tag{13}$$

The boundary conditions are treated between each successive iteration steps. Because of the refraction index mismatch at the air–tissue interface, the outgoing radiance is partly reflected on the boundary and only a fraction of that light escapes the medium. The internally reflected light contributes further to the photon propagation inside the medium, while the transmitted light enters the detectors. Using Fresnel's formula, the transmissivity T and reflectivity R are calculated at the boundary grid points for each ordinate ω_k and for the given refractive indices. The reflectivity R and the transmissivity T are defined as

$$R = \frac{\sin^2(\omega_{\text{trans}} - \omega_{\text{in}}) + \sin^2(\omega_{\text{trans}} + \omega_{\text{in}})}{2}, \tag{14}$$

$$T = 1 - R. \tag{15}$$

The angles ω_{trans}, which pertain to radiances escaping the object, are determined by Snell's law ($n_{\text{object}} \sin \omega_{\text{in}} = n_{\text{air}} \sin \omega_{\text{trans}}$) given the angle ω_{in} of the radiance, which hits the boundary inside the object. The angle $\omega_{\text{ref}} = -\omega_{\text{in}}$ is just the angle of the reflected radiance on the boundary inside the object. The transmitted and the reflected radiance are calculated with

$$\Psi^z_{\text{trans}} = T\Psi^z_{\text{in}}, \tag{16}$$

$$\Psi^z_{\text{ref}} = R\Psi^z_{\text{in}}. \tag{17}$$

The fluence Φ_{ij} on the boundary at the grid point (i, j), which enters the detector, is calculated for a given detector aperture AP using the transmitted radiance

$$\Phi(x_i, y_j) = \int_{\text{AP}} \Psi(x_i, y_j, \omega)\, \mathrm{d}\omega \approx \sum_{k=k_1}^{k=k_2} a_k \Psi_{k,i,j} = \Phi_{i,j}. \tag{18}$$

The weighting factors a_k are given by the extended trapezoidal rule [82], which provides the quadrature formula in this work.

3. Tissue phantoms and experimental setup

3.1. Tissue phantoms

The tissue phantoms were composed of clear epoxy resin into which silicon-dioxide (SiO_2) monospheres and ink were mixed. The scattering properties were adjusted by varying the concentration of the monospheres, while the absorption properties were controlled by the concentration of the ink. The g-factor could be varied by using spheres with different diameters. The optical properties of the phantoms were determined by two different methods. First, we employed an integrating sphere approach [84]. In this case, a thin slice of the phantom material was illuminated by a collimated laser beam, and the collimated, diffuse, and reflected light intensities were measured with an integrating sphere. Subsequently, a Monte-Carlo simulation was used to determine the absorption coefficient μ_a, scattering coefficient μ_s, and the anisotropy factor g. Secondly, a time-resolved transillumination technique was used. In this case, we measured the time-dependent distribution of the photons that traveled through a 2 cm thick slab of the

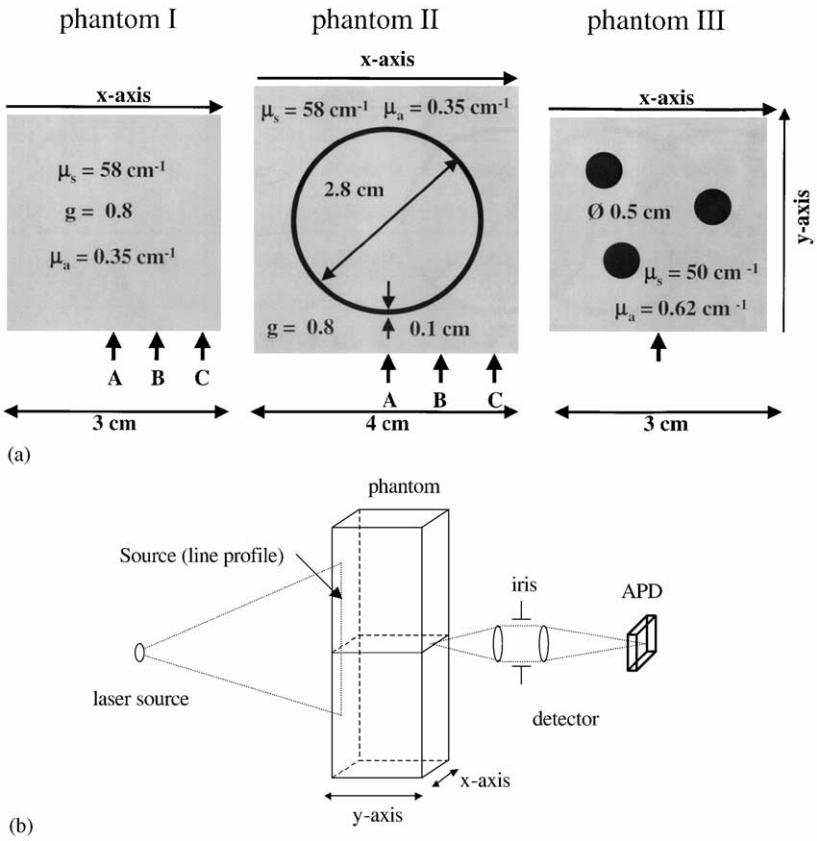

Fig. 1. (a) Geometry and optical properties of the three phantoms used in this study. (b) Details of the experimental setup.

medium. The transmitted pulse was compared to an analytical solution given by the diffusion equation for a slab geometry [85]. Thus, the reduced scattering coefficient $\mu_s' = (1-g)\mu_s$ and the absorption coefficient μ_a could be determined. Both methods gave similar results for μ_s' (within 4%), but showed larger differences for μ_a.

A total of three tissue phantoms were made of two different materials (Fig. 1a). First, a $3 \times 3 \times 14$ cm^3 homogeneous *Phantom I* was generated, which has a reduced scattering coefficient of $\mu_s' = 11.6 \pm 0.3$ cm^{-1}. The absorption coefficient was determined to be $\mu_a = 0.35 \pm 0.1$ cm^{-1}, with the Monte-Carlo technique giving higher absorption values than the time-resolved slab technique. Using the diameter of the monospheres ($d = 0.51$ μm) and the Mie-theory for light scattering, an anisotropy factor $g = 0.805$ was calculated. This is in agreement with the measurement obtained by the double-integrating-spheres approach, which provided a value of 0.8 ± 0.17. The refractive index of the resin is $n = 1.56$ at a wavelength of at $\lambda = 678$ nm [86].

From the same material we fabricated a $4 \times 4 \times 14$ cm^3 *Phantom II* that contained a ring with an inner diameter of 2.8 cm and an outer diameter of 3.0 cm. The ring was oriented along the 14-cm-long z-axis of the phantom and was filled with water to mimic void-like regions in tissues.

Finally, we prepared *Phantom III*, which had dimensions of $3 \times 3 \times 14\ \mathrm{cm}^3$ and contained 3 cylindrical voids with a diameter of 0.5 cm. The optical properties of the background medium were determined to be $\mu_s' = 7.5 \pm 0.3\ \mathrm{cm}^{-1}$, $\mu_a = 0.62 \pm 0.12$, and $g = 0.85$. The cylindrical holes were filled with water.

3.2. Light source

The phantoms were continuously illuminated with near-infrared light from a laser diode at $\lambda = 678$ nm. (Laser 2000 GmbH (Germany), LAS-670-20). As the phantoms were three-dimensional but the calculations were two-dimensional, we had to provide a z-axis-independent fluence. This was achieved by illuminating the phantom with an extended line source along the z-axis (Fig. 1b). The line source was realized by a laser diode with a light-emission angle of 20° along the z-axis, while along the x-axis the beam was collimated. In this way, the source consisted of a 6.0-cm long line with a width of 0.1 cm on the surface of the phantom. The source power applied to an area of $0.01\ \mathrm{cm}^2$ was 0.2 ± 0.01 mW. Measurements were taken with the line source positioned at different locations along the x-axis.

3.3. Light detection system

To measure the fluence Φ we used an avalanche photodiode APD (Hamamatsu, C5460-01). The detector was placed in the x–y plane of the phantom at the midpoint of the z-axis ($z = 7.0$ cm), and could be translated around the phantom along the x-axis and y-axis (Fig. 1a and b). The detection area at the boundary of the phantom was limited by a pinhole, which had a diameter of 0.1 cm. Two lenses projected the detection area onto the APD chip, whose diameter was 0.3 cm. An iris was placed in between the lenses, in order to adjust the aperture angle to $45 \pm 5.0^\circ$.

We used a lock-in technique to improve the signal-to-noise ratio. A frequency generator (Hewlett Packard, Waveform Generator 33120A) provided a sinusoidal modulation of the laser diode input with a frequency of 1014 Hz. The lock-in amplifier (Stanford Research Systems, Model SR 830) had a time constant of 3.0 s. An active bandwidth filter was connected between the detector output and lock-in amplifier input. The working point was set to 1014.0 Hz, with a bandwidth of 7.0 Hz. This efficiently suppressed the noise contributed by other frequencies, especially background light. At each detection spot the measuring time was approximately 10 s. During this time interval the measured fluence varied less than 0.2%. In general, signal levels were reproducible within 1.0% after removal and reinsertion of the sample into the measurement setup and realignment of both source and detector. The largest variations were observed for measurement points located close to the corners of the phantom.

4. Results

The calculated fluence was compared to the experimental data. We compared only relative fluence profiles on the boundary, not absolute fluences. This situation is typically encountered in clinical settings, because of the difficulty in calibrating the measurement system to an accurate

absolute value of the source strength [87]. The exact absolute value is difficult to determine because of often unknown and changing losses in the delivery- and collection-fiber systems, and inaccurate knowledge of the coupling coefficients between the skin and source and detector fibers. Thus, the measurement data and simulated data were normalized by their mean value to provide relative fluence profiles.

4.1. Homogeneous phantom

First, we compared measured and predicted fluence profiles of the homogeneous *Phantom I*. The numerical calculations with the upwind-difference discrete-ordinates method were performed on a 181×181 grid, with $\Delta x = \Delta y = 0.0167\ \text{cm} \cdot 1/\mu_s$. Thirty-two discrete ordinates were used for each calculation. The aperture of the APD detector was 45.0° in the x–y plane, therefore, the flux at the boundary in the simulation was summed over 4 ordinates. For the SOR method we chose an over-relaxation parameter $\rho = 1.1$. One forward calculation took approximately 700–1200 SOR iterations, which amounted to approximately 30 min of computation time on a Linux Workstation with a 450 MHz Pentium II processor.

The calculated fluence profile was compared to the measured data on the boundary of the phantom. The source was placed at three different positions along the edge of the phantom (A: 1.5 cm; B: 0.9 cm, and C: 0.3 cm) (Fig. 1a). For each source position measurements were taken along the side opposite of the source (x-axis) and the side adjacent to the source (y-axis) (see Figs. 1a and b). The separation between measurement points was 0.1 cm, resulting in 28 measurements on each side. Fig. 2 shows the experimental measurements and numerical calculations for the 3 different source positions. In Fig. 2a the results along the side opposite of the source are presented (x-axis), and Fig. 2b shows the results for the adjacent side (y-axis). The measurement error is not displayed because the error bars are smaller than the circles and diamonds in the figure.

To investigate how the predictions of the forward model depend on variations in optical properties, we studied the sensitivity of the numerical predictions to changes in the scattering coefficient, the absorption coefficient, and the anisotropy factor. In Fig. 3, numerical results are shown for the case of a fixed reduced scattering coefficient $\mu_s' = (1 - g)\mu_s$, but varying μ_s and g-factor. Fig. 4 displays results for different μ_s while all other parameters (μ_a and g) are kept constant. The absorption coefficient is varied in Fig. 5, and the anisotropy factor is varied in Fig. 6. In all figures the experimental results are given as open circles.

To evaluate the degree of agreement between numerical data, P, and experimental data, M, we calculated for each numerical set of data the average error given by

$$R = \frac{100}{N} \sqrt{\sum_{i}^{N} \frac{(M_i - P_i)^2}{M_i^2}}. \tag{19}$$

The R value is calculated separately for the x-axis data and y-axis data. Therefore the sum in Eq. (19) is taken over all detector readings along one side for one source. Table 1 shows the R values for all data shown in Figs. 3–6, plus additional measurements for the off-center sources, which are not displayed in the figures. The average error between numerical and experimental

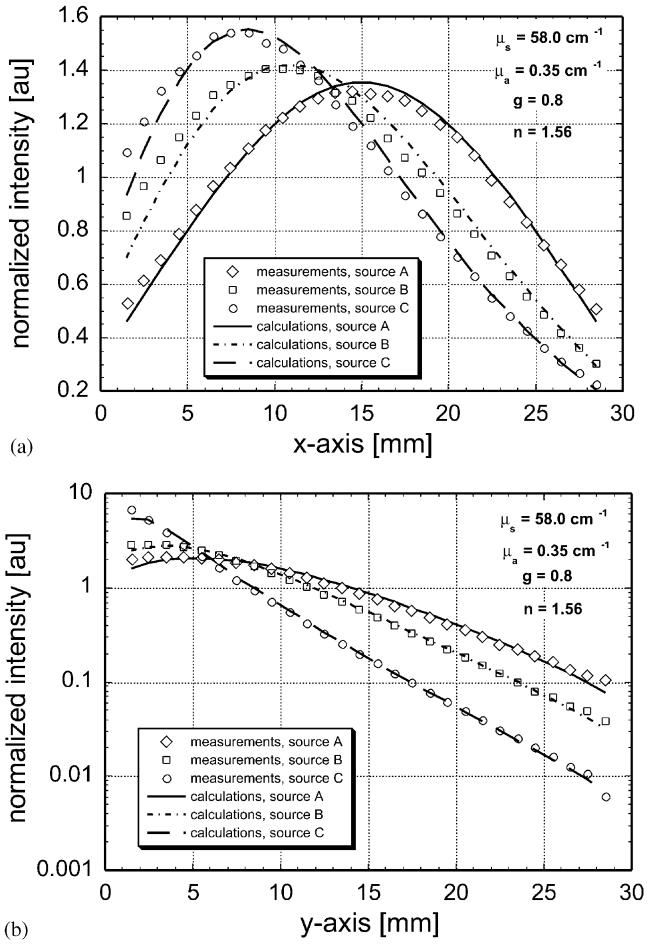

Fig. 2. Comparison of measured and calculated normalized fluence rates of the homogeneous phantom. Data were generated for three different source positions at different distances from the edge of the phantom (A: 1.5 cm, B: 0.9 cm, and C: 0.3 cm). For each source position, 28 detector points were measured along the x-axis (Fig. 2a) and along the y-axis (Fig. 2b).

data varies from 0.4% to 63.4%. For comparison, the average differences between two measurements on the same phantom with the same source–detector configuration are typically less than 0.2% along the side opposite the source (x-axis), and less than 1% along the side adjacent to the source (y-axis).

4.2. Phantoms with void-like regions

The results of measurements and predictions for *Phantom II*, which contained a water-filled, void-like ring, are shown in Figs. 7a and b. The forward calculations were done on a 241×241 grid, with a grid point separation of $\Delta x = \Delta y = 0.0167$ cm and 32 ordinates. The measurements

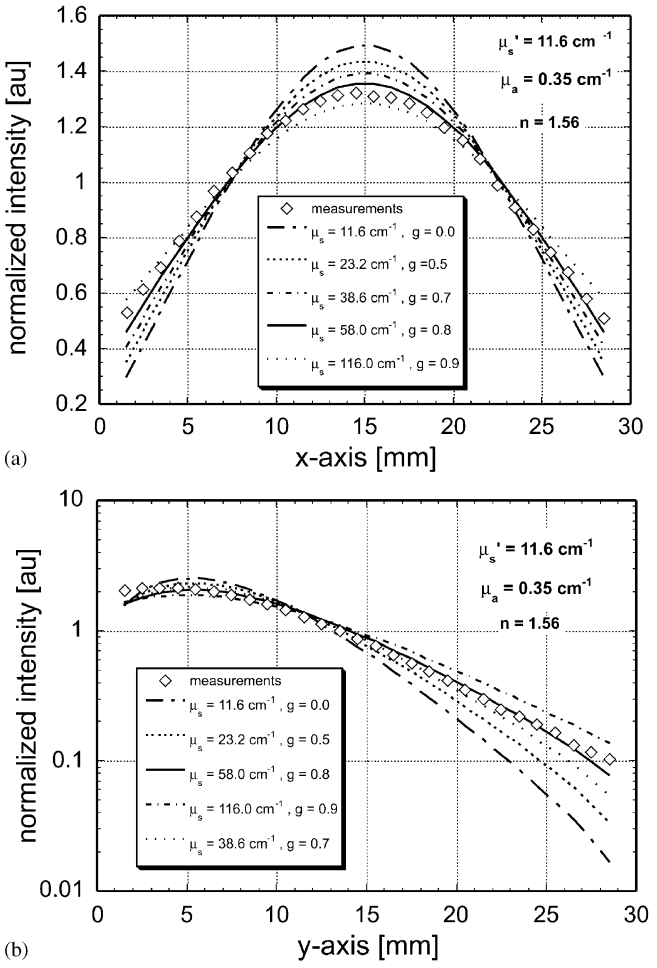

Fig. 3. Comparison of measured and calculated normalized fluence rates of the homogeneous phantom along the x-axis (Fig. 3a) and along the y-axis (Fig. 3b). Calculations were performed for different scattering coefficients and anisotropy factors, keeping all other optical parameters constant. The source was located at position A (see Fig. 1a).

were taken along the x-axis (Fig. 7a) and y-axis (Fig. 7b) at 38 detector points, with a spacing of 0.1 cm. Measurements were performed with the sources located at three different positions along the edge of the phantom (A: 2.0 cm, B: 1.2 cm, and C: 0.4 cm).

Figs. 8a and b show the results of measurements and simulations for *Phantom III*, which contained three cylindrical void-like regions. The simulations were performed on a 181×181 grid, with $\Delta x = \Delta y = 0.0167$ cm. Thirty-two discrete ordinates were used for each calculation. Results are shown for 15 measurements and calculations along the x-axis (Fig. 8a) and the y-axis (Fig. 8b), respectively. The source was located in the middle of the side opposite from where the x-axis measurements were taken (Fig. 1a).

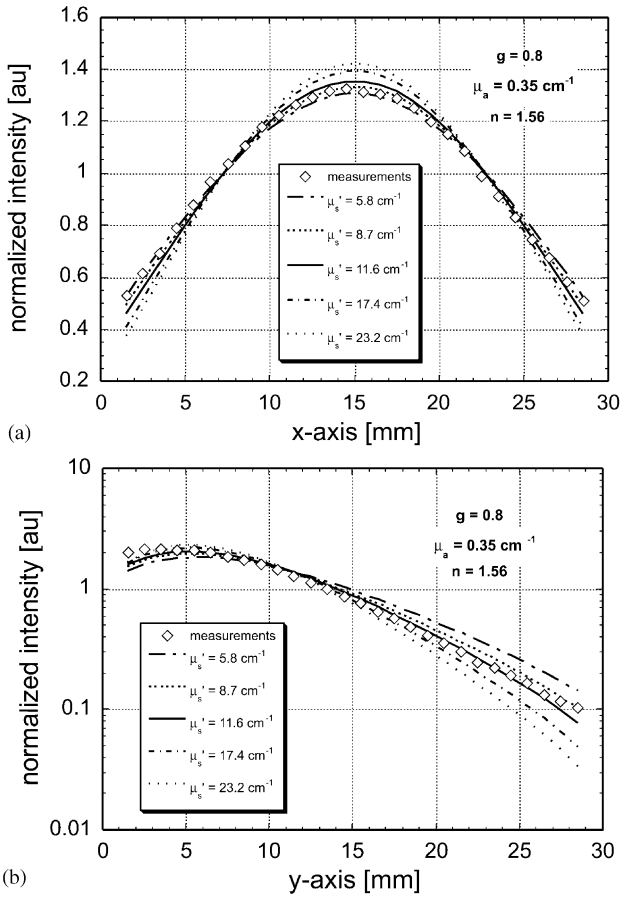

Fig. 4. Comparison of measured and calculated normalized fluence rates of the homogeneous phantom along the x-axis (Fig. 4a) and along the y-axis (Fig. 4b). Calculations were performed for different scattering coefficients keeping all other optical parameters constant. The source was located at position A (see Fig. 1a).

4.3. Discussion

Overall, we observed good agreement between measurements and calculations based on the assumed, independently verified, optical properties. For the homogeneous medium we found that the average error between the measured and calculated data for $\mu_s = 58.0\ \mathrm{cm}^{-1}$, $g = 0.8$, and $\mu_a = 0.35\ \mathrm{cm}^{-1}$ was between 0.82% and 1.83% for various source detector configurations (Fig. 2 and bold entries in Table 1). This error increases if other sets of optical properties are used as parameters for the forward code.

Several key observations can be made when evaluating the sensitivity of the predicted data for the homogeneous phantom to changes in the optical properties. For example, we found that the data along the y-axis is more sensitive to changes in optical properties than data along the x-axis. As can be seen in Table 1, the error between calculated and measured data is consistently higher for data sets taken on the side of the phantom as compared to data sets

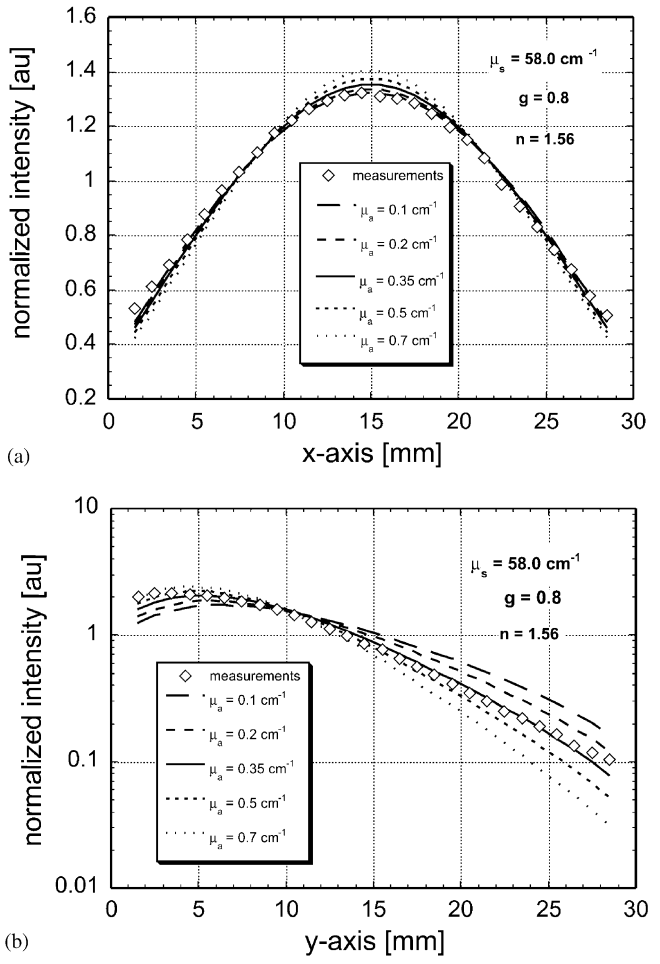

Fig. 5. Comparison of measured and calculated normalized fluence rates of the homogeneous phantom along the x-axis (Fig. 5a) and along the y-axis (Fig. 5b). Calculations were performed for different absorption coefficients, keeping all other optical parameters constant.

taken on the backside of the phantom. This suggests that for the successful reconstruction of optical properties it is advantageous to employ not only transmitted intensities measured on the backside of a target medium, but to include measurements on the sides of the object.

The importance of exact knowledge of both μ_s and g to characterize homogeneous media is illustrated in Fig. 3. In this graph, $\mu_s' = (1-g)\mu_s$ is fixed and different combinations of μ_s and g are used in the calculations of the intensity distribution along the x-axis and y-axis. It can be seen that only one combination ($\mu_s = 58\ \mathrm{cm}^{-1}$ and $g = 0.8$) fits the data well. In algorithms that employ the diffusion approximation to the radiative transfer equation only the parameter μ_s' appears as independent variable. However, in Fig. 3 all combination of μ_s and g yield the same μ_s', yet the results are not the same.

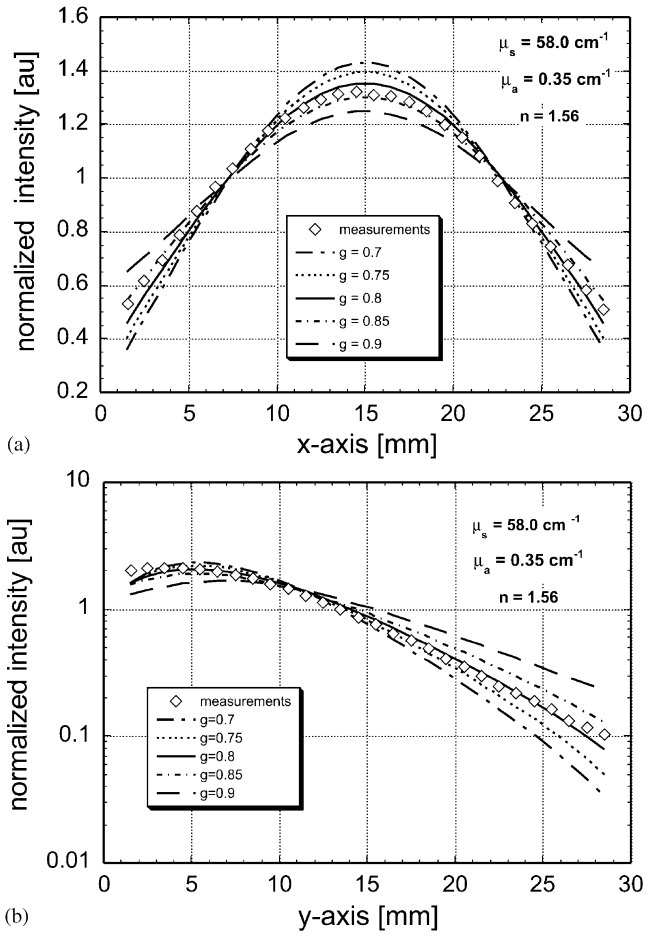

Fig. 6. Comparison of measured and calculated normalized fluence rates of the homogeneous phantom along the x-axis (Fig. 6a) and along the y-axis (Fig. 6b). Calculations were performed for different anisotropy factors, keeping all other optical parameters constant.

Figs. 2–6 and Table 1 can be used to estimate the sensitivity of the forward calculation to variations in the scattering coefficient, absorption coefficient, and g. For example, comparing Figs. 3–6 we notice that a change of g from 0.7 to 0.9, which is approximately $\pm 12\%$ about the optimal value of $g = 0.8$, results in a similar variability of the predicted data, as do changes of more than $\pm 50\%$ around the optimal value of either μ_a or μ_s. To quantify this observation, we plotted the average errors in Table 1 as a function of changes in the optical properties from the optimal values of $\mu_a = 0.35\ \mathrm{cm}^{-1}$, $\mu_s = 58\ \mathrm{cm}^{-1}$, and $g = 0.8$. Fig. 9 shows a representative result for the case where we take the average error for the measurements along the y-axis with the source in the center of the adjacent side (source A, in Table 1). We see that small variations in g lead to large increases in the error between measured and calculated data. For example a 5% deviation from the optimal value of $g = 0.8$ results in an average error increase between

Table 1
Average error R (Eq. (20)) between the measured and calculated normalized fluences along the x-axis and y-axis of the homogeneous phantom I for different optical parameters. The error R is calculated for three source positions A, B, and C at different distances from the edge of the phantom (A: 1.5 cm, B: 0.9 cm, and C: 0.3 cm)

	x-axis			y-axis		
	Source A	Source B	Source C	Source A	Source B	Source C
$\mu_s' = 11.6\ \mathrm{cm}^{-1}$ and $\mu_a = 0.35\ \mathrm{cm}^{-1}$						
$\mu_s = 11.6\ \mathrm{cm}^{-1}$ $g = 0.0$	3.27	3.78	4.97	7.83	9.79	12.81
$\mu_s = 23.2\ \mathrm{cm}^{-1}$ $g = 0.5$	2.35	2.51	3.1	5.39	6.96	10.02
$\mu_s = 38.6\ \mathrm{cm}^{-1}$ $g = 0.7$	1.57	1.66	1.79	3.17	3.77	5.87
$\mu_s = 58\ \mathrm{cm}^{-1}$ $g = 0.8$	**0.82**	**1.15**	**0.9**	**1.83**	**1.17**	**1.42**
$\mu_s = 116\ \mathrm{cm}^{-1}$ $g = 0.9$	0.98	1.74	1.47	4.46	7.74	18.14
$\mu_a = 0.35\ \mathrm{cm}^{-1}$ and $g = 0.8$						
$\mu_s' = 5.8\ \mathrm{cm}^{-1}$	0.51	1.43	1.24	5.93	9.52	21.95
$\mu_s' = 8.7\ \mathrm{cm}^{-1}$	0.47	1.2	0.85	2.79	3.67	7.11
$\mu_s' = 11.6\ \mathrm{cm}^{-1}$	**0.82**	**1.15**	**0.9**	**1.83**	**1.17**	**1.42**
$\mu_s' = 17.4\ \mathrm{cm}^{-1}$	1.51	1.6	1.89	3.68	4.58	6.75
$\mu_s' = 23.2\ \mathrm{cm}^{-1}$	2.03	2.2	2.9	5.44	6.97	9.75
$\mu_s = 58.0\ \mathrm{cm}^{-1}$ and $g = 0.8$						
$\mu_a = 0.1\ \mathrm{cm}^{-1}$	0.53	3.02	4.34	9.01	13.65	22.82
$\mu_a = 0.2\ \mathrm{cm}^{-1}$	0.62	2.11	2.58	4.9	6.58	10.10
$\mu_a = 0.35\ \mathrm{cm}^{-1}$	**0.82**	**1.15**	**0.9**	**1.83**	**1.17**	**1.42**
$\mu_a = 0.5\ \mathrm{cm}^{-1}$	1.08	1.15	2.01	3.59	4.31	5.6
$\mu_a = 0.7\ \mathrm{cm}^{-1}$	1.47	2.1	3.97	6.23	7.57	9.38
$\mu_s = 58.0\ \mathrm{cm}^{-1}$ and $\mu_a = 0.35\ \mathrm{cm}^{-1}$						
$g = 0.7$	2.22	2.4	3.05	5.53	7.12	10.09
$g = 0.75$	1.58	1.67	1.93	3.61	4.48	6.73
$g = 0.8$	**0.82**	**1.15**	**0.9**	**1.83**	**1.17**	**1.42**
$g = 0.85$	0.59	1.47	1.2	4.29	6.96	15.47
$g = 0.9$	1.88	2.44	2.48	11.5	20.57	63.33

measured and calculated data from 1.83% to 4%. The absorption and scattering coefficient have to deviate from their optimal values of $\mu_a = 0.35\ \mathrm{cm}^{-1}$ and $\mu_s = 58\ \mathrm{cm}^{-1}$ by about 40% to generate a similar increase in the average error R. Furthermore, note the qualitatively similar impact that variations of μ_a and μ_s have on the accuracy of the forward calculation.

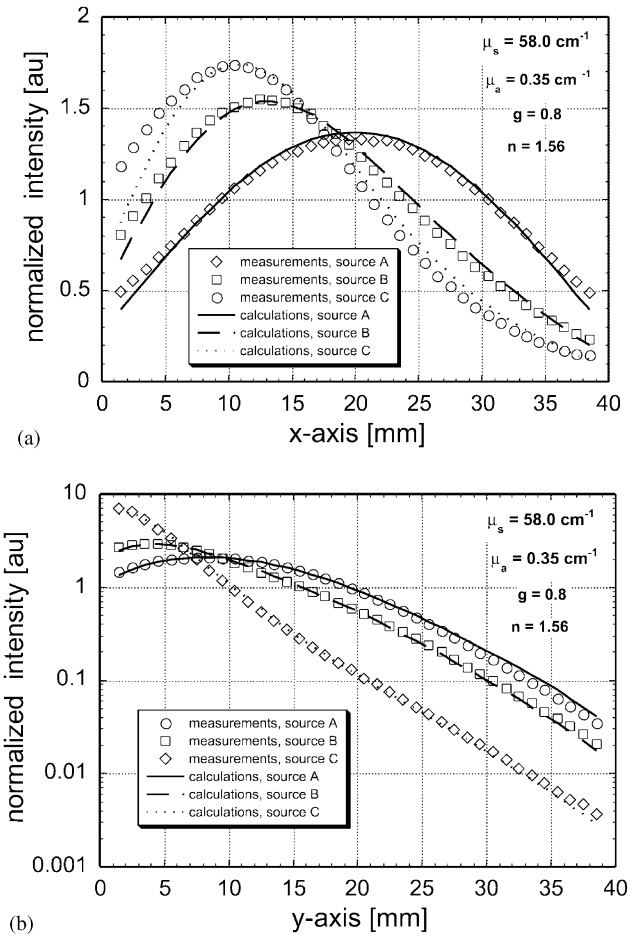

Fig. 7. Comparison of measured and calculated normalized fluence rates of tissue phantom II, which contains a water-filled ring. Data were generated for three different source positions at different distances from the edge of the phantom (A: 2.0 cm, B: 1.2 cm, and C: 0.4 cm, see Fig. 1a). For each source position 38 detector points were measured along the x-axis (Fig. 7a) and along the y-axis (Fig. 7b).

We also find good agreement between measurements and predictions for the Phantoms II and III, which contained a void-like ring and three cylindrical water inclusions, respectively (Figs. 7 and 8). The average error R (Eq. (19)) varied between 0.81% and 4.43% for all source–detector configurations. This experimentally confirms our previous numerical findings that, unlike diffusion-theory-based codes, algorithms based on the equation of radiative transfer can accurately describe light propagation in media that contain void-like regions.

While good overall agreement between measurement and simulated data was found, some differences remain. There appear to be two main reasons for this. First, the experimental determination of the optical properties of the phantom that was used to validate the algorithm is subject to errors. Different methods, such as single integrating sphere, double integrating sphere, time-resolved technique, time-independent methods, etc., all have advantages and disadvantages

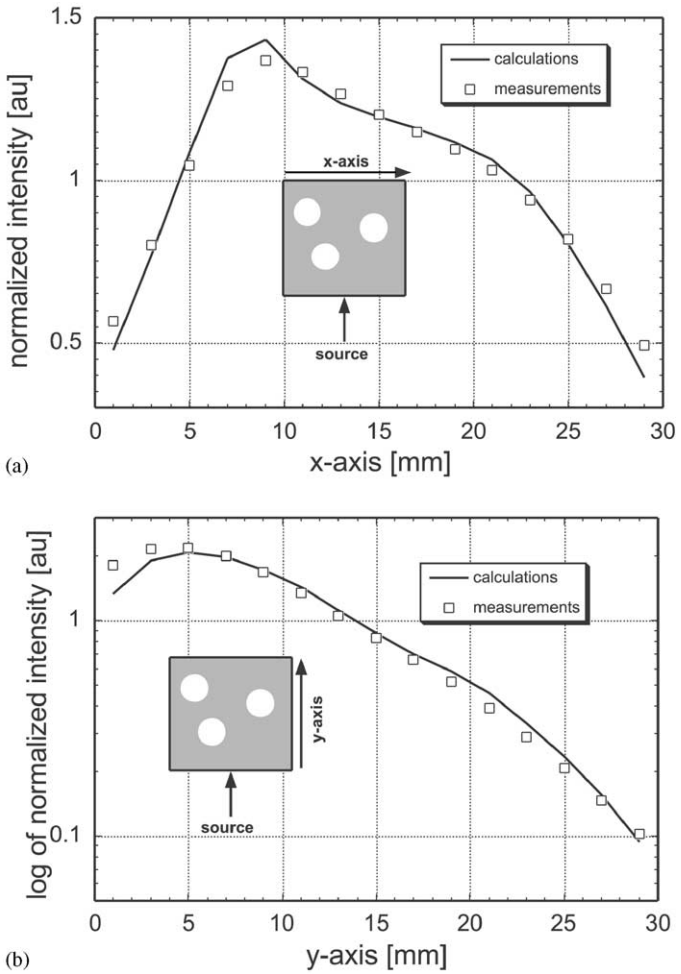

Fig. 8. Comparison of measured and calculated normalized fluence rates of tissue phantom III, which contained three water-filled, void-like cylinders. Shown are measurements along the x-axis (Fig. 8a) and along the y-axis (Fig. 8b), as indicated in the inset.

and often lead to different results, especially for μ_a. For example, over the last 15 years several groups have measured the optical properties of Intralipid, which is a milk-like emulsion of fat particles [88–91]. Flock et al. summarizes these studies by giving the mean and standard deviation of all cited works combined. They find that the optical properties of 10% Intralipid at 633 nm are $\mu_a = (0.027 \pm 0.154)\ \mathrm{cm}^{-1}$, $\mu_s' = (144 \pm 9)\ \mathrm{cm}^{-1}$, and $g = (0.75 \pm 0.18)$ [91]. Therefore, in agreement with our observations, they find that μ_a values differ strongly from method to method, while μ_s' is determined rather consistently. Unfortunately no single technique has been accepted within the biomedical optical community as a standard for measuring optical properties. Currently, no National Institute of Standards in the world is providing optical phantoms with certified optical properties. Therefore, the validation of any algorithm remains somewhat uncertain, especially with respect to μ_a.

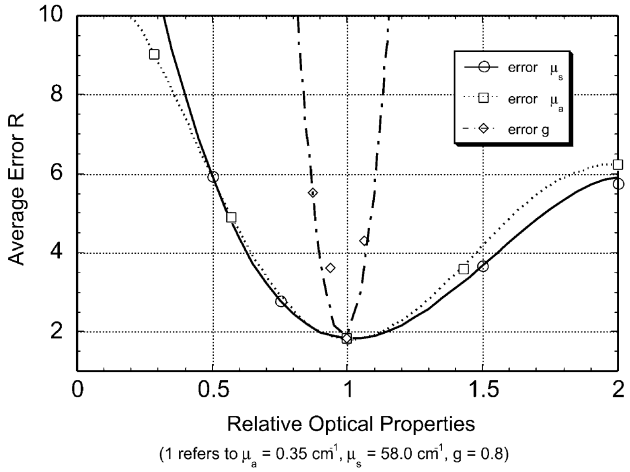

Fig. 9. Average error R (Eq. (19)) for different optical properties, of the homogeneous phantom I. Measurements were taken along the y-axis for source position A.

Second, the upwind-difference, discrete-ordinates scheme used in this work is, like any other finite-difference scheme, an approximation to the equation of radiative transfer. In our study the spatial derivative was discretized to first-order. Higher-order discretizations that yield more complex formulas may further improve the match between the experimental and measured data. A detailed analysis of how much higher-order approximations improve current results, remains a subject for further study.

5. Summary

Most of the currently employed image reconstruction schemes in optical tomography are model-based algorithms, in which numerically predicted data are compared to measured data. The predictions are obtained by forward models that describe light propagation in tissue. The most commonly employed model is based on the diffusion equation, which is an approximation to the more generally applicable equation of radiative transfer. Several groups have shown in the past that diffusion-equation based algorithms fail to describe photon propagation in void-containing media. These types of media play an important role, for example, in studies of light propagation in the human head and joints. The goal of this two-part study is to develop an image reconstruction algorithm based on the equation of radiative transfer.

In part I we presented an upwind-difference, discrete-ordinates algorithm that solves the time-independent equation of radiative transfer for media with an arbitrary distribution of optical properties. Because Fresnel boundary conditions and anisotropic scattering were explicitly considered, it was for the first time possible to test the performance of this algorithm against experimental data. Fluence measurements on homogeneous tissue-like phantoms were performed and showed good agreement with calculated detector readings. An analysis of the influence of the various optical properties on detector readings showed that without an accurate knowledge of g, the measured data could not be predicted accurately. Furthermore, fluence measurements

performed on the surface of tissue phantoms that contained void-like regions were performed, and these measurements also agreed well with the simulated data.

Acknowledgements

The authors would like to thank Dr. Uwe Sukowski, Physikalisch-Technische Bundesanstalt Berlin, Germany for the phantom preparation. Furthermore, we would like to thank Dr. Ntziachristos and Dr. Chance, University of Pennsylvania, Philadelphia, for the determination of the optical properties with a time-resolved measurement system. We also would like to thank Avraham Bluestone and Dr. Harry Graber, State University of New York—Downstate Medical Center (SUNY DMC), for their helpful comments concerning this manuscript.

This work was supported in part by the National Institute of Arthritis and Musculoskeletal and Skin Diseases, a part of the National Institute of Health (grant #R01 AR46255-01), the Whitaker Foundation (grant #98-0244), the City of New York Council Speaker's Fund for Biomedical Research: Towards the Science of Patient Care, and the Dean's Office of the College of Medicine at the State University of New York Downstate Medical Center (SUNY DMC).

References

[1] Chance B, Alfano RR, Tromberg BJ, Tamura M, Sevick-Muraca EM. Optical tomography and Spectroscopy iv. Proceeding of the SPIE vol. 4250, 2001.
[2] Chance B, Alfano RR, Tromberg BJ. Optical tomography and spectroscopy of tissue III. Proceeding of the SPIE vol. 3597, 1999.
[3] Chance B, Alfano RR, Katzir A. Optical tomography and spectroscopy of tissue II: theory, instrumentation, model, and human studies. Proceeding of the SPIE vol. 2979, 1997.
[4] Kirkpatrick PJ. Use of near-infrared spectroscopy in the adult. Philos Trans Roy Soc London Ser B: Biol Sci 1997;352:701–5.
[5] Henson LC, Calalang C, Temp JA, Ward DS. Accuracy of a cerebral oximeter in healthy volunteers under conditions of isocapnic hypoxia. Anesthesiology 1998;88:58–65.
[6] Benaron DA, Vanhouten JP, Cheong W, Kermit EL, King RA. Early clinical results of time-of-flight optical tomography in a neonatal intensive care unit. Proc SPIE 1995;2389:582–96.
[7] Cheong WF, Vanhouten JP, Kermit EL, Machold TR, Stevenson DK, Benaron DA. Pilot comparison of light-based optical tomography versus ultrasound for real-time imaging of neonatal intraventricular hemorrhage. Pediatr Res 1996;39:1189.
[8] Hoshi Y, Oda I, Wada Y, Ito Y, Yamashita Y, Oda M, Ohta K, Yamada Y, Tamura M. Visuospatial imagery is a fruitful strategy for the digit span backward task: a study with near-infrared optical tomography. Cognitive Brain Res 2000;9:339–42.
[9] Maki A, Yamashita Y, Watanabe E, Koizumi H. Visualizing human motor activity by using non-invasive optical topography. Front Med Biol Eng 1996;7:285–97.
[10] Hirth C, Obrig H, Valdueza J, Dirnagl U, Villringer A. Simultaneous assessment of cerebral oxygenation and hemodynamics during a motor task. A combined near infrared and transcranial Doppler sonography study. Adv Exp Med Biol 1997;411:461–9.
[11] Hock C, Villringer K, Müller-Spahn F, Hofmann M, Schuh-Hofer S, Heekeren H, Wenzel R, Dirnagl U, Villringer A. Near infrared spectroscopy in the diagnosis of Alzheimer's disease. Ann New York Acad Sci 1996;777:22–9.
[12] Fallgatter AJ, Roesler M, Sitzmann L, Heidrich A, Müller TJ, Strik WK. Loss of functional hemispheric asymmetry in Alzheimer's dementia assessed with near-infrared spectroscopy. Brain Res Cognitive Brain Res 1997;6:67–72.

[13] Prapavat V, Runge W, Mans J, Krause A, Beuthan J, Müller G. The development of a finger joint phantom for the optical simulation of early inflammatory rheumatic changes. Biomed Tech 1997;42:319–26.
[14] Klose A, Prapavat V, Minet O, Beuthan J, Müller G. RA diagnostics applying optical tomography in frequency-domain. Proc SPIE 1997;3196:194–204.
[15] Nioka S, Yung Y, Shnall M, Zhao S, Orel S, Xie C, Chance B, Solin L. Optical imaging of breast tumor by means of continuous waves. Adv Exp Med Biol 1997;411:227–32.
[16] Alfano RR, Demos SG, Gayen SK. Advances in optical imaging of biomedical media. Ann New York Acad Sci 1997;820:248–70.
[17] Franceschini MA, Moesta KT, Fantini S, Gaida G, Gratton E, Jess H, Mantulin WW, Seeber M, Schlag PM, Kaschke M. Frequency-domain techniques enhance optical mammography: Initial clinical results. Proc Natl Acad Sci USA 1997;94:6468–73.
[18] Parker JA. Image reconstruction in radiology. Boca Raton, FL: CRC Press, 1990.
[19] Walker SA, Fantini S, Gratton E. Image reconstruction by backprojection from frequency domain optical measurements in highly scattering media. Appl Opt 1997;36:170–9.
[20] Colak SB, Papaioannou DG, 't Hooft GW, van der Mark MB, Schomberg H, Paasschens JCJ, Melissen JBM, van Asten NAAJ. Tomographic image reconstruction from optical projections in light-diffusing media. Appl Opt 1997;36:180–213.
[21] Hielscher AH, Klose AD, Hanson KM. Gradient-based iterative image reconstruction scheme for time resolved optical tomography. IEEE Trans Med Imag 1999;18(3):262–71.
[22] Arridge SR, Schweiger M. A gradient-based optimisation scheme for optical tomography. Opt Express 1998;2(6):213–26.
[23] Arridge SR, Hebden JC. Optical imaging in medicine: II. Modelling and reconstruction. Phys Med Biol 1997;42:841–53.
[24] Arridge SR. Photon-measurement density functions. Part I: analytical forms. Appl Opt 1995;24:7395–409.
[25] Arridge SR, Schweiger M. Photon measurement density functions. Part 2: finite-element-method calculation. Appl Opt 1995;34:8026–37.
[26] Schweiger M, Arridge SR. A system for solving the forward and inverse problems in optical spectroscopy and imaging. In: Alfano RR, Fujimoto JG, editors. Advances in optical imaging and photon migrations, OSA Trends in Optics and Photonics Series, vol. 2. Washington DC: Optical Society of America, 1996. p. 263–8.
[27] Barbour RL, Graber HL, Wang Y, Chang JH, Aronson R. A perturbation approach for optical diffusion tomography using continous-wave and time-resolved data. In: Müller G, editor. Medical optical tomography. SPIE Institute for Advanced Optical Technologies Series, vol. IS11, SPIE Optical Engineering Press, Bellingham, WA, 1993. p. 87–120.
[28] Graber HL, Chang J, Aronson R, Barbour RL. A perturbation model for imaging in dense scattering media: Derivation and Evaluation of Imaging Operators. In: Müller G, editor. Medical optical tomography. Bellingham, WA: SPIE Optical Engineering Press, vol. IS11, 1993. p. 121–43.
[29] Barbour RL, Graber HL, Chang JW, Barbour SLS, Koo PC, Aronson R. MRI-guided optical tomography: prospects and computation for a new imaging method. IEEE Comput Sci Eng 1995;2:63–77.
[30] Yao YQ, Wang Y, Pei YL, Zhu WW, Barbour RL. Frequency-domain optical imaging of absorption and scattering distributions by Born iterative method. J Opt Soc Am A 1997;14:325–42.
[31] Paulsen KD, Jiang H. Spatially varying optical property reconstruction using a finite element diffusion equation approximation. Med Phys 1995;22:691–701.
[32] Paulsen KD, Jiang H. Enhanced frequency domain optical image reconstruction in tissues through total variation minimization. Appl Opt 1996;35:3447–58.
[33] Jiang H, Paulsen KD, Osterberg UL. Optical image reconstruction using DC data: simulations and experiments. Phys Med Biol 1996;41:1483–98.
[34] Jiang H, Paulsen KD, Osterberg UL, Pogue BW, Patterson MS. Simultaneous reconstruction of optical absorption and scattering maps in turbid media from near-infrared frequency-domain data. Opt Lett 1995;20:2128–30.
[35] Jiang HB, Paulsen KD, Osterberg UL, Pogue PW, Patterson MS. Optical image reconstruction using frequency domain data: Simulations and experiments. J Opt Soc Am A 1996;13:253–66.

[36] O'Leary MA, Boas DA, Chance B, Yodh AG. Experimental images of heterogeneous turbid media by frequency-domain diffusion-photon tomography. Opt Lett 1995;20:426–8.
[37] Paithankar DY, Chen AU, Pogue BW, Patterson MS, Sevick-Muraca EM. Imaging of fluorescent yield and lifetime from multiply scattered light reemitted from random media. Appl Opt 1997;36:2260–72.
[38] Klibanov MV, Lucas TR, Frank RM. A fast and accurate imaging algorithm in optical diffusion tomography. Inverse Problems 1997;13:1341–61.
[39] Saquib SS, Hanson KM, Cunningham GS. Model-based image reconstruction from time-resolved diffusion data. Proc SPIE 1997;3034:369–80.
[40] Hielscher AH, Klose A, Catarious Jr D, Hanson KM. Tomographic imaging of biological tissue by time-resolved, model-based, iterative, image reconstructions. In: Alfano RR, Fujimoto JG, editors. OSA Trends in Optics and Photonics: Advances in optical imaging and photon migration II, vol. 21. Washington DC: Optical Society of America, 1998. p. 156–61.
[41] Klose AD, Hielscher AH. Iterative reconstruction scheme for optical tomography based on the equation of radiative transfer. Med Phys 1999;26(8):1698–707.
[42] Roy R, Sevick-Muraca EM. Truncated Newton's optimization scheme for absorption and fluorescence optical tomography. Part I: theory and formulation. Opt Express 1999;4(10):353–71.
[43] Ye JC, Webb KJ, Bouman CA, Millane RP. Optical diffusion tomography by iterative-coordinate-descent optimization in a Bayesian framework. J Opt Soc Am A 1999;16(10):2400–13.
[44] Ye JC, Webb KJ, Millane RP, Downar TJ. Modified distorted Born iterative method with an approximate Frechet derivative for optical diffusion tomography. J Opt Soc Am A 1999;16(7):1814–27.
[45] Eppstein MJ, Dougherty DE, Troy TL, Sevick-Muraca EM. Biomedical optical tomographyusing dynamic parameterization and Bayesian conditioning on photon migration measurements. Appl Opt 1999;38(10): 2138–51.
[46] Ishimaru A. Diffusion of light in turbid material. Appl Opt 1989;28(12):2210–5.
[47] Ishimaru A. Wave propagation and scattering in random media. New York: Academic Press, 1978.
[48] van de Hulst HC. Light scattering by small particles. New York: Wiley, 1957.
[49] van de Hulst HC. Multiple light scattering. New York: Academic Press, 1980.
[50] Groenhuis RAJ, Ferwerda HA, Ten Bosch JJ. Scattering and absorption of turbid materials determined from reflection measurements. 1: Theory. Appl Opt 1983;22(16):2456–62.
[51] Groenhuis RAJ, Ten Bosch JJ, Ferwerda HA. Scattering and absorption of turbid materials determined from reflection measurements. 2: Measuring method and calibration. Appl Opt 1983;22(16):2463–7.
[52] Profio AE. Light transport in tissue. Appl Opt 1989;28(12):2216.
[53] Aronson R, Barbour RL, Lubowsky J, Graber H. Application of transport theory to infra-red medical imaging. In: Greenberg W, Ploewczak J, editors. Modern mathematical methods in transport theory. Basel: Birkhäuser, 1991. P. 64–75.
[54] Yoon G, Welch AJ, Motamedi M, van Gemert MCJ. Development and application of three-dimensional light distribution model for laser irradiated tissue. IEEE J Quant Electron 1987;QE-23(19):1721–33.
[55] Hielscher AH, Alcouffe RE, Barbour RL. Comparison of finite-difference transport and diffusion calculations for photon migration in homogeneous and heterogeneous tissue. Phys Med Biol 1998;43:1285–302.
[56] Firbank M, Arridge SR, Schweiger M, Delpy DT. An investigation of light transport through scattering bodies with non-scattering regions. Phys Med Biol 1996;41:767–83.
[57] Dehghani H, Delpy DT, Arridge SR. Photon migration in non-scattering tissue and the effects on image reconstruction. Phys Med Biol 1999;44(12):2897–906.
[58] Ripoll J, Nieto-Vesperinas M, Arridge SR, Dehghani H. Boundary conditions for light propagation in diffusive media with nonscattering regions. J Opt Soc Am A 2000;17(9):1671–82.
[59] Arridge SR, Dehghani H, Schweiger M, Okada E. The finite element model for the propagation of light in scattering media: a direct method for domains with nonscattering regions. Med Phys 2000;27(1):252–65.
[60] Firbank M, Arridge SR, Schweiger M, Delpy DT. An investigation of light transport through scattering bodies with non-scattering regions. Phys Med Biol 1996;41(4):767.
[61] Okada E, Firbank M, Schweiger M, Arridge SR, Cope M, Delpy DT. Theoretical and experimental investigation of near-infrared light propagation in a model of the adult head. Appl Opt 1997;36(1):21–32.

[62] Schweiger M, Arridge SR. Optical tomographic reconstruction in a complex head model using a priori region boundary information. Phys Med Biol 1999;44(11):2703.
[63] Klose A, Hielscher AH, Hanson KM, Beuthan J. Three-dimensional optical tomography of a finger joint model for diagnostic of rheumatoid arthritis. Proc SPIE 1998;3566:151–60.
[64] Arridge SR, Dehghani H, Schweiger M, Okada E. The finite element model for the propagation of light in scattering media: a direct method for domains with nonscattering regions. Med Phys 2000;27:252–64.
[65] Riley J, Dehghani H, Schweiger M. Arridge SR, Ripoll J, Nieto-Vesperinas M. #D Optical tomography in the presence of void regions. Optics Express 2000;7(13):462–67.
[66] Dorn O. A transport-backtransport method for optical tomography. Inverse Problems 1998;14:1107–30.
[67] Case KM, Zweifel PF. Linear transport theory. Massachussetts: Addison-Wesley, 1967.
[68] Duderstadt JJ, Martin WR. Transport theory. New York: Wiley, 1979.
[69] Davis B. Neutron transport theory. London: Oxford University Press, 1957.
[70] Welch AJ, Van Gemert MJC. Optical-thermal response of laser irradiated tissue. New York: Plenum Press 1995. p. 144–8.
[71] Lewis EE, Miller WF. Computational Methods of neutron transport. New York: Wiley, 1984.
[72] Sanchez R, McCormick NJ. A Review of neutron transport approximations. Nucl Sci Eng 1982;80:481–535.
[73] Carlson BG, Lathrop KD. Transport theory—the method of discrete ordinates. In: Greenspan H, Kelber CN, Okrent D, editors. Computing methods in reactor physics. New York: Gordon and Breach, 1968.
[74] Lathrop KD. Discrete-ordinates methods for the numerical solution of the transport equation. Reactor Technol 1972;15(2):107–34.
[75] Richtmyer RD, Morton KW. Difference methods for initial-value problems. New York: Wiley, 1967.
[76] Lathrop KD. Spatial differencing of the transport equation: positivity vs. accuracy. J Comp Phys 1969;4:475.
[77] Reed WH. New difference schemes for the neutron transport equation. Nucl Sci Eng 1971;46:309–14.
[78] Madsen NK. Convergent centered difference schemes for the discrete ordinate neutron transport equations. SIAM J Num Anal 1975;12(2):164–76.
[79] Alcouffe RE. An adaptive weighted diamond differencing method for three-dimensional xyz geometry. Trans Am Nuc Soc 1993;68 A:206–12.
[80] Alcouffe RE. Diffusion synthetic acceleration: method for the diamond differenced discrete ordinates equation. Nuc Sci Eng 1977;64:344–52.
[81] Sewell G. The numerical solution of ordinary and partial differential equations. San Diego: Academic Press, 1988.
[82] Press WH, Teukolsky SA, Vetterling WT, Flannery BP. Numerical recipes in C. New York: Cambridge University Press, 1992.
[83] Ames WF. Numerical methods for partial differential equations. New York: Academic Press, 1977.
[84] Roggan A, Albrecht H, Dörschel K, Minet O, Müller G. Experimental set-up and Monte-Carlo model for the determination of optical properties in the wavelength range 330–1100 nm. Proceedings of SPIE 1995;2323: 21–36.
[85] Patterson MS, Chance B, Wilson BC. Time-resolved reflectance and transmittance for the non-invasive measurement of tissue optical properties. Appl Opt 1989;28:2331–6.
[86] Firbank M, Oda M, Delpy D. An improved design for a stable and reproducible phantom material for use in near-infrared spectroscopy and imaging. Phys Med Biol 1995;40:955–61.
[87] Boas DA, Gaudette T, Arridge SR. Simultaneous imaging and optode calibration with diffuse optical tomography. Opt Express 2001;8:263–70.
[88] Star WM, Marijnissen JPA, Jansen H, Keijzer M, van Gemert MJC. Light dosimetry for photodynamic therapy by whole bladder wall irradiation. Photchem Photobiol 1987;46:619–24.
[89] Moes CJM, van Gemert MJC, Star WM, Marijnissen JPA, Prahl SA. Measurements and calculations of the energy fluence rate in a scattering and absorbing phantom at 633 nm. Appl Opt 1989;28:2292–6.
[90] van Staveren HJ, Moes CJM, van Marle J, Prahl SA, van Gemert MJC. Light scattering in Intralipid-10% in the wavelength range of 400–1100 nm. Appl Opt 1991;30:4507–14.
[91] Flock ST, Jacques SL, Wilson BC, Star WM, van Gemert MJC. Optical properties of Intralipid: A phantom medium for light propagation studies. Lasers Surg Med 1992;12:510–9.